BMC Medical Imaging

RESEARCH Open Access

A radiomics nomogram based on multiparametric MRI for diagnosing focal cortical dysplasia and initially identifying laterality

Shi-qi Chen[1], Liang Wei[2], Keng He[1], Ya-wen Xiao[1], Zhao-tao Zhang[1], Jian-kun Dai[3], Ting Shu[1], Xiao-yu Sun[1], Di Wu[1], Yi Luo[1], Yi-fei Gui[1] and Xin-lan Xiao[1*]

Abstract

Background Focal cortical dysplasia (FCD) is the most common epileptogenic developmental malformation. The diagnosis of FCD is challenging. We generated a radiomics nomogram based on multiparametric magnetic resonance imaging (MRI) to diagnose FCD and identify laterality early.

Methods Forty-three patients treated between July 2017 and May 2022 with histopathologically confirmed FCD were retrospectively enrolled. The contralateral unaffected hemispheres were included as the control group. Therefore, 86 ROIs were finally included. Using January 2021 as the time cutoff, those admitted after January 2021 were included in the hold-out set ($n=20$). The remaining patients were separated randomly (8:2 ratio) into training ($n=55$) and validation ($n=11$) sets. All preoperative and postoperative MR images, including T1-weighted (T1w), T2-weighted (T2w), fluid-attenuated inversion recovery (FLAIR), and combined (T1w+T2w+FLAIR) images, were included. The least absolute shrinkage and selection operator (LASSO) was used to select features. Multivariable logistic regression analysis was used to develop the diagnosis model. The performance of the radiomic nomogram was evaluated with an area under the curve (AUC), net reclassification improvement (NRI), integrated discrimination improvement (IDI), calibration and clinical utility.

Results The model-based radiomics features that were selected from combined sequences (T1w+T2w+FLAIR) had the highest performances in all models and showed better diagnostic performance than inexperienced radiologists in the training (AUCs: 0.847 VS. 0.664, $p=0.008$), validation (AUC: 0.857 VS. 0.521, $p=0.155$), and hold-out sets (AUCs: 0.828 VS. 0.571, $p=0.080$). The positive values of NRI (0.402, 0.607, 0.424) and IDI (0.158, 0.264, 0.264) in the three sets indicated that the diagnostic performance of Model-Combined improved significantly. The radiomics nomogram fit well in calibration curves ($p>0.05$), and decision curve analysis further confirmed the clinical usefulness of the nomogram. Additionally, the contrast (the radiomics feature) of the FCD lesions not only played a crucial role in the classifier but also had a significant correlation ($r=$ -0.319, $p<0.05$) with the duration of FCD.

*Correspondence:
Xin-lan Xiao
jx_xiaoxinlan@sina.com

Full list of author information is available at the end of the article

Conclusion The radiomics nomogram generated by logistic regression model-based multiparametric MRI represents an important advancement in FCD diagnosis and treatment.

Keywords Epilepsy, FCD, Radiomics, Nomogram, Precision medicine

Introduction

Focal cortical dysplasias (FCDs) are common malformations of cerebral cortical development that were first observed in epilepsy patients by Taylar et al. in 1971 [1, 2]. The histopathological characteristics of FCD include abnormalities of the white matter, cortical dyslamination, and large unusual neurons, and half of the patients presented with balloon cells [3]. FCD is the most common cause of drug resistance in patients with focal epilepsy. Focal resection is the most common method used to treat drug-refractory epilepsy patients with FCD [4]. If these patients do not receive timely intervention, they suffer an increased risk of premature death [5].

Magnetic resonance imaging (MRI) is a noninvasive technique that can provide rich structural and functional information about the whole brain. Previous results based on structural T1-weighted (T1-W) and T2-weighted (T2-W) MRI showed cortex thickening, white/gray matter (GM/WM) junction blurring, hyperintensity within white/gray matter, abnormal architecture of the subcortical layer, and unnatural sulus or gyrus patterns in FCD patients by visual inspection [6].

Several postprocessing methods based on voxel and surface-based morphological analysis have emerged to improve the visibility of FCD on MRI [7, 8]. In voxel-based morphometry (VBM), several feature maps (e.g., thickness, extension, junction maps) are computed voxelwise, which enhances the typical features of FCD and increases the sensitivity of MRI for detection [9, 10]. Martin et al. found that VBM contributed more to the detection of temporal lobe structural malformation cortical dysplasias than visual examination. In 13 patients, the results of VBM were consistent with postoperative histopathological findings (72.2%), unlike the 55.6% observed with visual inspection [11].

Despite its practicality and robustness, VBM approaches have certain inherent limitations. First, they cannot evaluate spatial relationships across the cortical surface, and any registration errors can result in subtle lesions being missed [12]. Second, in accordance with earlier studies, because the whole processing of VBM is performed by a fully automated MATLAB script called the Morphometric Analysis Programme (MAP), yield and diagnostic confidence also depend on the reader's experience [13].

Surface-based morphometry (SBM) can be used to estimate a variety of features, such as cortex volume, thickness, and area, as well as gyrification. Unlike VBM, SBM includes additional analysis of morphometric features (such as sulcal depth and curvature) that are known to be abnormal in patients with FCD; thus, the anatomical relationships across the folded cortex are not neglected [14, 15]. This novel classifier was used to identify 89% (17 of 19) of small, histologically proven FCDs that were overlooked on conventional MRI [16]. However, SBM approaches also have some drawbacks, such as unavoidable and unknown biases that may arise from the sex, age, race, etc., of the included healthy controls [17]. Therefore, there are some limitations in practical clinical use.

Radiomics is a new approach that is used to extract high-throughput image features from radiographic images, which provides a powerful tool for modern medicine by improving accurate diagnosis and treatment [18]. In the terms of epilepsy diagnosis, radiomic features from the hippocampus offer valuable insights into the pathophysiology of TLE and can aid in distinguishing TLE patients from individuals without epilepsy [19, 20]. Beyond the hippocampus, radiomic features extracted from regions outside the hippocampus have been particularly useful in identifying patients with hippocampal sclerosis and those with negative MRI findings but still exhibit clinical symptoms of TLE [21]. This approach has shown to be valuable in improving the accuracy of TLE diagnosis. Radiomics is not limited to diagnosis; it is pivotal in predicting drug treatment efficacy for TLE. By merging radiomic features from imaging data with extensive clinical information, predictive models emerge. These models offer clinicians valuable insights into expected treatment outcomes, enabling personalized and more effective interventions [22]. These studies show that radiomics features could aid in identifying TLE. However, radiomics analyses performed in FCD-related epilepsy patients are still rare. Additionally, it is known that studies on the duration of epilepsy suggest that changes in structural integrity may be progressive over the course of the disease [23], illustrating that the correlation between the duration of the disease and the MR findings improves diagnosis and assists in prognosis. Therefore, such a correlation should be studied.

Nomograms are statistical instruments utilized in clinical practice to assess the likelihood of a particular outcome. Prognostication is crucial in guiding treatment decisions and determining appropriate follow-up intervals. Nomograms offer an advantage over traditional staging systems by incorporating a wider array of clinicopathologic variables, thereby providing a more comprehensive prognosis. Additionally, nomograms

present statistical predictions in a visually intuitive format, enhancing their utility for clinicians [24].

The purpose of this study was to investigate whether a radiomics nomogram that depended on a conventional multiparametric MR radiomics-based logistic regression model could be used to differentiate FCD patients and healthy controls. In addition, we explored the correlations between the selected features and the duration of the FCD with the goal of aiding in the identification of FCD using MRI visual detection.

Methods and materials

Participant selection

The institutional review board of the Second Affiliated Hospital of Nanchang University approved this retrospective study, and the requirement to obtain informed consent was waived. Figure 1 shows a flow chart of patient recruitment and grouping. First, sixty-seven patients were retrospectively selected between July 2017 and May 2022. All of them were drug-refractory epilepsy patients and received focal resection treatment. All the involved patients were pathologically confirmed to have FCD according to the guidelines of the International League Against Epilepsy (ILAE). The clinical data of the sixty-seven patients were collected from the Electronic Hospital Information System (EHIS) of our hospital. Then, patients ($n=4$) with Engel class III or IV (reduction of seizure frequency>75%, or reduction of seizure frequency<75%), a history of encephalitis ($n=1$), severe traumatic brain injury ($n=1$), diffuse brain atrophy ($n=1$), preoperative EEG evidence of bilateral epileptiform discharges ($n=5$), excessive postoperative brain tissue deformation ($n=7$), and poor-quality neuroimaging data ($n=5$) were excluded. Finally, forty-three patients were included.

Using January 2021 as the time cutoff point, patients were divided into two groups, with patients before January 2021 used as the training and validation sets and patients after January 2021 used as the hold-out set.

Thirty-three patients who belonged to the training and validation sets and underwent surgery before January 2021 received telephone follow-ups in January 2022; thus, all patients had more than one year of follow-up. Seizure recurrence is mainly limited to the first postoperative year and has been a reliable predictor of long-term outcomes in patients with FCD [25]. Therefore, the minimum follow-up period in our study was one year. The phone interview was performed by one of the authors using the Engel system, which is used to evaluate seizure outcomes following surgery for epilepsy by focusing on the patient's daily lives [26, 27]. Thus, complete resection of the epileptogenic lesion of the thirty-three patients in the training and validation sets was ensured.

Image acquisition

MRI data were obtained for forty-three FCD patients using a 3.0T MR scanner (Discovery MR 750 W; GE Healthcare, Milwaukee, WI, USA) with a 24-channel head coil. Three sequences were acquired with the following parameters:

Brain volume imaging (BRAVO): TR/TE 8.2/3.1 ms; field of view 256×256, section thickness 1 mm, matrix 256×256, flip angle 12°.

Axial T2w imaging: TR/TE 9786/108.7 ms; field of view 260×260, section thickness 3 mm, matrix 240×240, flip angle 142°.

Axial T2FLAIR imaging: TR/TE 8000/142.3 ms; field of view 260×260, section thickness 3 mm, matrix 256×256, flip angle 160°.

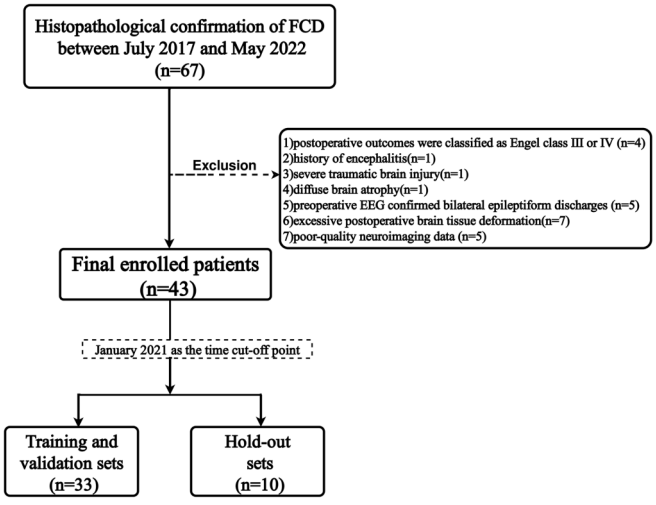

Fig. 1 Flow diagram of patient inclusion and allocation to the training, validation, and hold-out sets

Development and testing of the Radiomics Model

Figure 2 shows the workflow of the development and testing of the radiomics model. The workflow followed a radiomics-specific reporting guideline [28] (checklist attached as Supplementary Materials 1).

Region of interest definition and segmentation

All images were resampled to 1 mm x 1 mm x 1 mm and were then utilized to delineate the region of interest (ROI) by using 3D Slicer (v 4.11.2; https://www.slicer.org).

Grayscale images can be automatically aligned to each other using intensity-based registration methods. General registration (Elastix) (in SlicerElastix extension) is recommended by 3D Slicer's user guide (https://slicer.readthedocs.io/en/latest/user_guide/registration.html), and its default registration presets work without the need for any parameter adjustments. Therefore, for the training and validation sets, we utilized the Elastix module to register preoperative and postoperative images of patients, facilitating subsequent segmentation steps.

A radiologist with five years of experience in diagnosing diseases of the central nervous system (CNS) manually marked the brain resection area depending on the area of operation and preoperative multisequence MR images as the ROI (Supplementary Materials 2). Then, the ROI was mirrored and transformed to the contralateral hemisphere using the 3D Slicer transforms module, yielding two ROIs for a single patient. ROIs in the contralateral unaffected hemisphere were included as the control group. Finally, we obtained 66 ROIs from 33 patients. The same radiologist randomly chose half of the patients and repeated ROI segmentation twice in an 8-week period. The reproducibility was subject to analysis with the intraclass correlation coefficient (ICC). All ROIs were reviewed by a radiologist with 37 years of experience in diagnosing CNS diseases to ensure the accuracy of the segmentation. Notably, all patients included in the training and validation sets were classified as Engel class I or II, which guaranteed that the epileptogenic zone was totally included in the ROI.

The hold-out set was used to demonstrate the robustness of the radiomics-based model and further evaluate whether the model could determine the laterality of the lesion. We extracted brain structures using the Brain Extraction Tool (BET) [29] via the FMRIB Software Library (FSL). Data regarding nonbrain (e.g., skull, dura, eyes, extracerebral cerebrospinal fluid, and major veins) tissue from the whole head were removed from the source images. Then, the whole left and right cerebral hemispheres were obtained as ROIs from the preoperative MR images using a semiautomatic method. Finally, we obtained 20 ROIs from 10 patients.

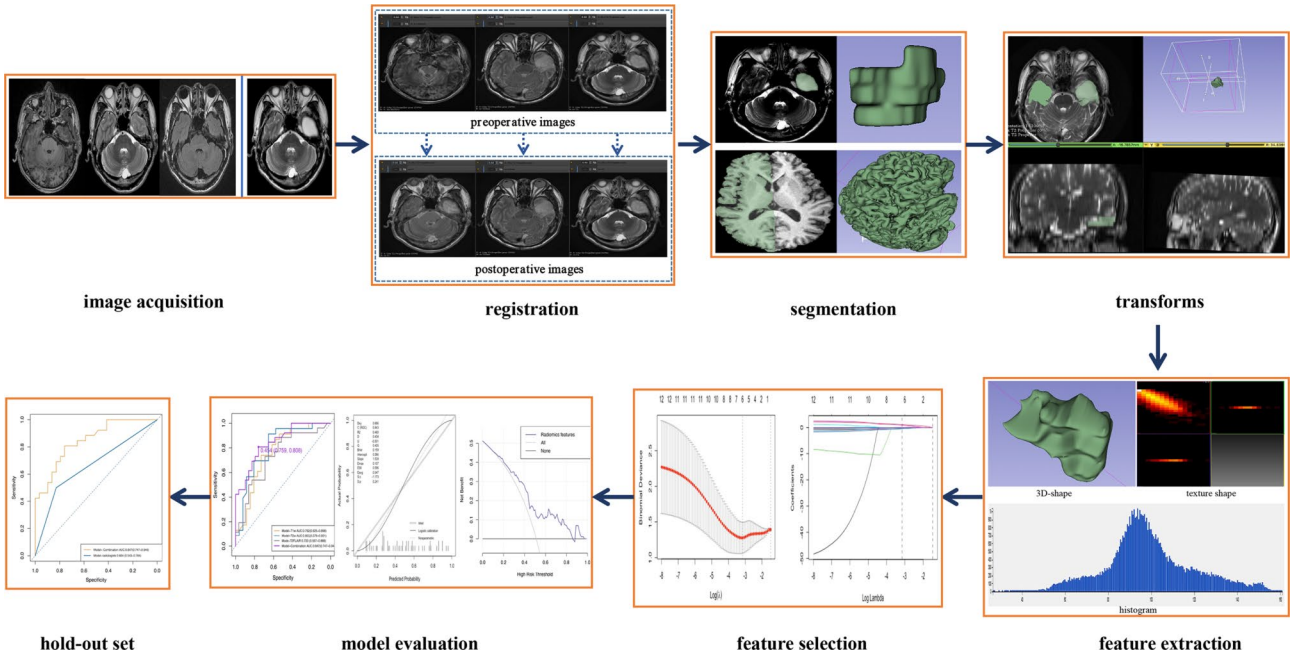

Fig. 2 The workflow of the development and testing of the radiomics model. First, the preoperative and postoperative images were registered. The top row shows the pre- and postoperative images before the registration of the three sequences, with a 50% transparency overlay. The bottom row shows the pre- and postoperative images after registration, also with 50% transparency overlap. Second, ROIs were segmented manually, mirrored, and transformed to the contralateral hemisphere for radiomic analysis. Third, radiomics features were extracted. Fourth, in the training set, the most relevant features were selected by LASSO methods with penalty parameter tuning. The multivariate logistic model was established. Fifth, ROC curves, calibration plots, and decision curve analysis were used to evaluate the performance of the models. Sixth, the multivariate logistic model was tested with the hold-out set

Radiomics feature extraction

The radiomic features were extracted from the segmented volumes in accordance with the image biomarker standardization initiative (IBSI) guidelines [30]. Feature extraction was processed on the PyRadiomics module embedded in the 3D Slicer Radiomics Extension Pack (v.4.11.2 https://www.slicer.org/). No image intensity or voxel size normalization was needed since all MR images had identical grayscale and voxel sizes. Image intensity discretization was conducted with fixed intensity bin widths of 25 (default in PyRadiomics). High-frequency or low-frequency wavelet filters, Laplacian of Gaussian (LoG) filters with different λ-parameters (λ=0.5, 1.0, 1.5, 2.0), and wavelet-based processes were used for preprocessing the original MR images, which can be used to accurately obtain the detailed features of the images. We then extracted the original MR images and the radiomics characteristics of segmented lesions, including the first-order characteristics based on preprocessed image pixel values, the gray-level dependence matrix (GLDM), gray-level cooccurrence matrix (GLCM), gray-level run length matrix (GLRLM), gray-level size zone matrix (GLSZM) and neighborhood-tone difference matrix (NGTDM), which described the morphological characteristics of lesions and the internal and surface texture features. Finally, we used Z-scores to standardize all features on the same scale.

Radiomic feature selection and model establishment

First, features with high stability (ICC>0.80) were retained for further analysis. Next, a total of 66 ROIs were split into two sets at an 8:2 ratio. Subsequent analysis was executed in R software (version 4.1.3; http://www.rproject.org). We used the least absolute shrinkage and selection operator (LASSO) method [31], which is suitable for dimensionality reduction in high-dimensional data, with penalty parameter tuning conducted by four-fold cross-validation to select the optimal diagnostic features from the training set. Then, features with nonzero coefficients were retained as the most important features in the multivariate logistic regression model.

FCD diagnostic model evaluation

Receiver operating characteristic (ROC) curves were plotted, and an AUC was used to quantify the discriminative efficacy of all radiomics models based on single sequences and combined sequences. The AUC with 95% CI and the sensitivity, specificity, and accuracy were calculated.

Development and validation of the nomogram

Nomograms are frequently employed in disease prognosis or diagnosis to condense complex statistical models into a single, patient-specific probability estimate for events such as death or recurrence. These user-friendly graphical tools assist clinical decision-making during patient encounters. For each predictor variable, find the corresponding value on the horizontal axis of the nomogram and determine the associated points. Sum the points for all variables to obtain the total points. Draw a line from the total points on the nomogram to the predicted probability scale on the vertical axis. The point where the line intersects the scale corresponds to the estimated probability of the outcome [32]. The radiomics nomogram was generated using the model that had the most satisfactory diagnostic performance. Next, calibration plots were used to examine the diagnostic performance of the nomogram in both the training and validation sets. The nonsignificant unreliability U test was used to estimate the agreement between nomogram-diagnosed FCD and actual FCD from the calibration curves. Decision curve analysis was conducted to determine the clinical usefulness of the nomogram by quantifying the net benefits at different threshold probabilities in all cohorts [33].

Hold-out test

The trained radiomics-based logistic regression model was applied to the hold-out set.

Development of the radiologist model

One radiologist with 5 years of experience in assessing CNS diseases and a 3-year resident in training independently provided a diagnosis based on the MR images without knowing any other clinical or laboratory information. In the case of any discrepancy, a consensus was reached after discussion. Diagnoses based on the MR images were included in univariate analysis to generate a logistic regression model.

Statistical analysis

Statistical analysis was performed using R software (version 4.1.3; http://www.rproject.org). The distribution of the data was evaluated by the Kolmogorov–Smirnov test and Shapiro–Wilk test. The duration of patients in the validation set was compared using Student's t test and was described as the mean [standard deviation (SD)]. Nonnormally distributed variables (age, duration of patients in training, and hold-out sets) were analyzed by the Mann–Whitney U test and were described as medians [interquartile ranges (IQRs)]. Categorical variables (sex, affected hemisphere, Engel system, MRI representation, pathology) were analyzed by the chi-square test or Fisher's exact test and were described as absolute numbers (n) and proportions (%). ROC curve analysis was used to evaluate the accuracy, sensitivity, and specificity of this model in differentiating FCD patients and healthy controls. The AUC of the ROC curves was compared by

the Delong method. The net reclassification improvement (NRI) and the integrated discrimination improvement (IDI) were used to further assess improvement in model performance [34].

We used the "glmnet" package for the analysis of LASSO logistic regression, which was applied to the radiomics features. The "rms" package was used to generate nomogram and calibration curves. The packages "pROC" and "ggplot" were used to plot ROC curves, and the AUC represents the optimal cutoff threshold value that was computed. The package "reportROC" were used to calculate CI. The package "PredictABEL" was used to calculate the NRI and IDI. The "generalhoslem" and "rmda" packages were used to calculate the Hosmer–Lemeshow test and DCA, respectively.

Because the disease duration of whole sets did not conform to a normal distribution, the correlation between the duration of FCD and the selected features was tested by Spearman's test. All statistical tests were two-sided, and *P* values of <0.05 were regarded as significant.

Result

Patient characteristics

The baseline characteristics of the patients with lesions and healthy controls are shown in Table 1. The training set included 29 nonaffected ROIs and 26 affected ROIs, and the validation set included 4 nonaffected ROIs and 7 affected ROIs. The hold-out set was composed of 10 nonaffected ROIs and 10 affected ROIs. There were no significant differences in the variables age or gender between the training and validation sets (Table 1, $p>0.05$), indicating that the use of random seeds to group the total data was reasonable. These variables also did not differ between the FCD lesion patients and healthy controls in the training and validation sets, as they did in the hold-out set.

Radiomics feature extraction

A total of 1223 radiomics features were extracted from the ROIs of the single T1w, T2w, and T2-FLAIR images, and 3669 radiomics features of the combined-sequence images, including 14 shape features, 18 first-order features, and 75 texture features [gray-level dependence matrix (GLDM, 14), gray-level cooccurrence matrix

Table 1 Clinical characteristics in the training, validation and hold-out sets

	Training set (*N* = 55)		*P*-value	Validation set (*N* = 11)		*P*-value	Hold-out set (*N* = 20)		*P*-value
	Control (*N* = 29)	Lesion (*N* = 26)		Control (*N* = 4)	Lesion (*N* = 7)		Control (*N* = 10)	Lesion (*N* = 10)	
Sex			0.956			0.689			1.000
Female	11 (37.9)	11 (42.3)		3 (75.0)	3 (42.9)		3 (30.0)	3 (30.0)	
Male	18 (62.1)	15 (57.7)		1 (25.0)	4 (57.1)		7 (70.0)	7 (70.0)	
age (median [IQR])	20.00 [16.00,35.00]	21.00 [14.75, 34.00]	0.846	26.75 (7.68)	30.00 (13.13)	0.665	21.50 [19.25,30.75]	21.50 [19.25, 30.75]	1.000
duration (median[IQR])/ (mean (SD))	NA	8.00 [3.25, 12.25]		NA	14.71 (14.49)		NA	4.50 [3.00, 7.50]	
hemi (%)	NA			NA			NA		
Left		9 (34.6)			5 (71.4)			8 (80.0)	
Right		17 (65.4)			2 (28.6)			2 (20.0)	
Engel (%)	NA			NA			NA		
I		16 (61.5)			4 (57.1)			5 (50.0)	
II		10 (38.5)			3 (42.9)			4 (40.0)	
III		0			0			1 (10.0)	
MRI (%)	NA			NA			NA		
MRI-positive		10 (38.5)			2 (28.6)			3 (30.0)	
MRI-negtive		16 (61.5)			5 (71.4)			7 (70.0)	
pathology (%)	NA			NA			NA		
FCDIA		4 (15.4)			0			1 (10.0)	
FCDIB		4 (15.4)			2 (28.6)			1 (10.0)	
FCDIIA		3 (11.5)			2 (28.6)			0	
FCDIIB		3 (11.5)			0			0	
FCDIIIA		4 (15.4)			1 (14.3)			2 (20.0)	
FCDIIIB		0			0			2 (20.0)	
FCDIIIC		2 (7.7)			0			2 (20.0)	
N		6 (23.1)			2 (28.6)			2 (20.0)	

Table 2 Four groups of radiomics features selected from four groups MR images were showd

Model-T1w	Model-T2w	Model-T2FLAIR	Model-Combination
log-sigma-0.5-mm-3D_glcm_Autocorrelation	log-sigma-2-0-mm-3D_ firstorder_Mean	log-sigma-0-5-mm-3D_firstorder_Median	T2-wavelet-HHL_ glcm Correlation
log-sigma-2-0-mm-3D_ firstorder_Mean	wavelet-HHL_glcm_Correlation	log-sigma-1-5-mm-3D_firstorder_Median	T2-log-sigma-1-0-mm-3D_ngtdm_ Contrast
wavelet-HLL_gldm_ LargeDependenceLowGrayLevelEmphasis		log-sigma-1-5-mm-3D_ glcm_Imc2	T2-log-sigma-1-0-mm-3D_gldm_ DependenceVariance
wavelet-HLL_glszm_ ZoneVariance		log-sigma-2-0-mm-3D_ firstorder_10Percentile	T1-wavelet-HLL_ glszm_ ZoneVariance
wavelet-HLL_glrlm_ShortRunLowGray-LevelEmphasis			T1-wavelet-HLL_ gldm_LargeDepen-denceLowGray-LevelEmphasis
Wavelet-HHL_gldm_DependenceEntropy			T2FLAIR-log-sigma-0-5-mm-3D_fir-storder_ Median

Table 3 The radiomics features selected from the model-combination ranking according to each feature weight

Features($N=6$)	Modality	Coefficient	OR
wavelet-HHL_glcm_Correlation	T2	1.09021095	2.97490156
log-sigma-1-0-mm-3D_ngtdm_Contrast	T2	0.89270456	2.44172452
log-sigma-1-0-mm-3D_gldm_DependenceVariance	T2	-0.0915470	0.91251842
wavelet-HLL_glszm_ZoneVariance	T1	-0.1222656	0.88491330
wavelet-HLL-gldm_LargeDependenceLowGrayLevelEmphasis	T1	-0.4392388	0.64452682
log-sigma-0-5-mm-3D_firstorder_Median	T2FLAIR	-0.4839260	0.61635879

(GLCM, 24), gray-level run length matrix (GLRLM, 16), gray-level size zone matrix (GLSZM, 16) and neighborhood-tone difference matrix (NGTDM, 5)], 744 higher-order features following wavelet transformation and 372 higher-order features following LoG transformation.

Radiomic feature selection and signature construction

Features with intraobserver ICCs < 0.80 were discarded. Therefore, 951 features with high stability from the T1w images, 880 features from the T2w images, and 954 features from the T2FLAIR images were obtained.

For the single MR sequence, six features highly correlated with identifying FCD were extracted and selected from the T1w images, two from the T2w images, and four from the T2FLAIR images by using LASSO regression (Table 2). Six features (Table 3) were selected from the combined MRI by using the same method (Fig. 3a, b).

These final features were used to build four radiomics models through multivariate logistic regression.

Model performance evaluation

The detailed performance results of the different models are listed in Table 4. The ROC curves showed that Model-Combination had the highest performances in all models, with AUCs of 0.847 (95% CI 0.747–0.946) and 0.857 (95% CI 0.618-1.000) in the training and validation sets, respectively. In the single sequence, Model-T2w had the most satisfying performances, with AUCs of 0.805 (95% CI 0.679–0.931) and 0.814 (95% CI 0.606-1.000) in the training set and validation sets, respectively. Model-T2FLAIR [AUCs: 0.733 (95% CI 0.597–0.868), 0.714 (95% CI 0.374-1.000)] and Model-T1w [AUCs: 0.762 (95% CI 0.625–0.898), 0.671 (95% CI 0.400-0.943)] had poor performances, especially with low AUCs in the validation set (Fig. 4). Model-Combination showed excellent diagnostic performance compared with Model-radiologists in the training (AUC: 0.847). VS. 0.664; $p=0.008$), validation (AUC: 0.857 VS. 0.521; $p=0.155$), and hold-out sets (AUCs: 0.828 VS. 0.571; $p=0.080$) (Fig. 5). The specific results obtained after cross-validation are reported in Supplementary Material 4.

Although the Delong tests did not reveal significant differences between the ROC curves of Model-Combination and Model-radiologists in the validation and the hold-out sets, Model-Combination yield the 1.143 (95% CI: 0.410, 1.876, $p=0.002$), 1.192 (95% CI: 0.484, 1.901, $p<0.000$) of NRI (Continuous) and 0.264 (95% CI: 0.012, 0.517 $p=0.040$), 0.264 (95% CI: 0.046, 0.482, $p=0.018$) of IDI in validation and hold-out sets, respectively, which are positive values, indicating that the diagnostic performance of Model-Combination improved significantly. Table 5 shows reclassification among Model-Combination and Model-radiologists in training, validation, and hold-out sets.

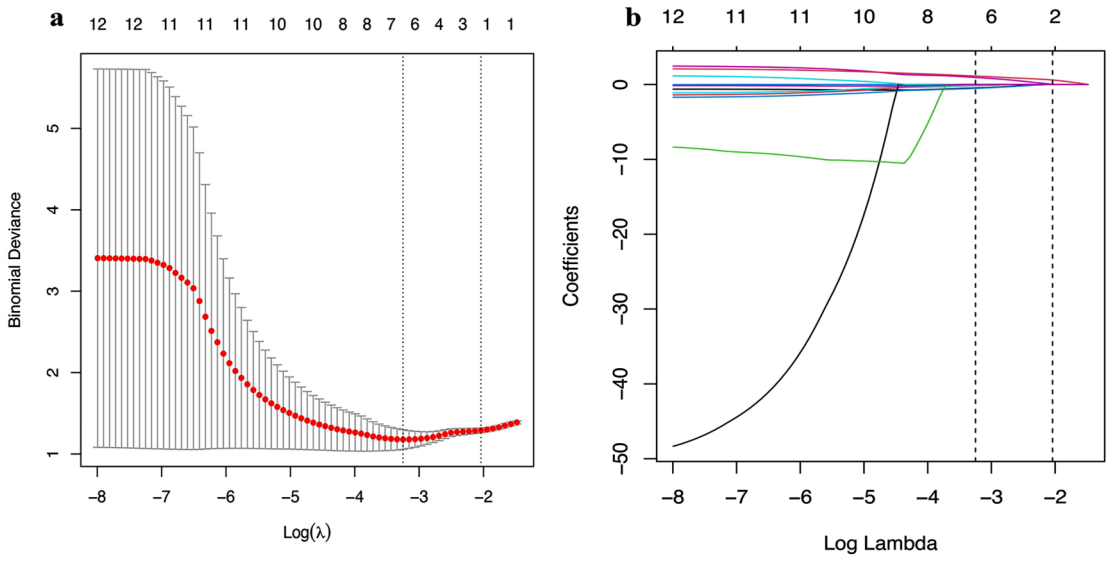

Fig. 3 FCD candidate variable selection using LASSO regression. (**a**) Binomial deviation graph of the optimal tuning parameter (λ) in the LASSO model. (**b**) LASSO coefficient profiles of the six possible influencing factors

Table 4 Performance of MRI-based radiomics features in diagnosing FCD in the training, validation and hold-out sets

Modality	Sets	AUC(95%CI)	Sen	Spe	Acc
Model-T1w	Training	0.762(0.625–0.898)	0.739(0.599–0.879)	0.731(0.471–0.871)	0.694(0.584–0.804)
	Validation	0.671(0.400-0.943)	0.600(0.418–0.782)	0.857(0.756–0.958)	0.706(0.455–0.957)
Model-T2w	Training	0.805(0.679–0.931)	0.654(0.550–0.758)	0.913(0.900-0.926)	0.694(0.583–0.805)
	Validation	0.814(0.606-1.000)	0.600(0.489–0.711)	1.000(0.750-1.000)	0.706(0.602–0.810)
Model-T2FLAIR	Training	0.733(0.597–0.868)	0.731(0.611–0.851)	0.690(0.580–0.800)	0.582(0.450–0.714)
	Validation	0.714(0.374-1.000)	0.429(0.318–0.540)	1.000(0.850-1.000)	0.364(0.182–0.546)
Model-Combination	Training	0.847(0.747–0.946)	0.808(0.704–0.912)	0.759(0.629–0.889)	0.782(0.640–0.924)
	Validation	0.857(0.618-1.000)	0.714(0.607–0.821)	1.000(0.750-1.000)	0.818(0.666–0.970)
Model-radiologists	Training	0.664(0.543–0.784)	0.828(0.715–0.941)	0.500(0.250–0.750)	0.327(0.214–0.440)
	Validation	0.521(0.148–0.893)	0.375(0.274–0.476)	0.667(0.426–0.908)	0.182(0.173–0.191)
Model-Combination	Hold-out	0.828(0.619-1.000)	1.000(0.768-1.000)	0.667(0.497–0.837)	0.850(0.750–0.950)
Model-radiologists	Hold-out	0.571 (0.363–0.778)	0.364(0.262–0.466)	0.778(0.574–0.982)	0.550(0.389–0.711)

Development and validation of the nomogram

The nomogram based on the Model-Combination diagnostic model including its 6 diagnostic variables is presented in Fig. 6a. Calibration curves (Fig. 6b, c) indicated that the diagnosis probabilities of the nomogram were closely aligned with actual FCD estimates in both the training (p=0.152) and validation sets (p=0.732). Decision curve analysis (DCA) indicated that Model-Combination had the most clinical utility, as shown in the plot in Fig. 6d.

RQS score

The Radiomics Quality Score (RQS) is a scoring system proposed by Lambin in 2017 and is commonly used for evaluating the methodologic quality of radiomics research [35]. One of the radiologists with most experience in radiomics research based on the RQS system derived an RQS score for our study of 18 (Supplementary Materials 5).

Correlation between Radiomics features and duration of FCD

In the correlation analysis, only the contrast (the radiomics feature belonging to texture features) of the FCD lesions had a statistically significant correlation (r = -0.319, p<0.05) with the duration of FCD (Fig. 7), while the correlations of the other features did not (Supplementary Materials 6).

Discussion

In our study, four radiomics models based on T1w, T2w, and T2-FLAIR images and their combination were developed to diagnose FCD, and the combined model (AUC, 0.847/0.857; sensitivity, 0.808/0.714; specificity, 0.759/1.000; and accuracy, 0.782/0.818) outperformed all

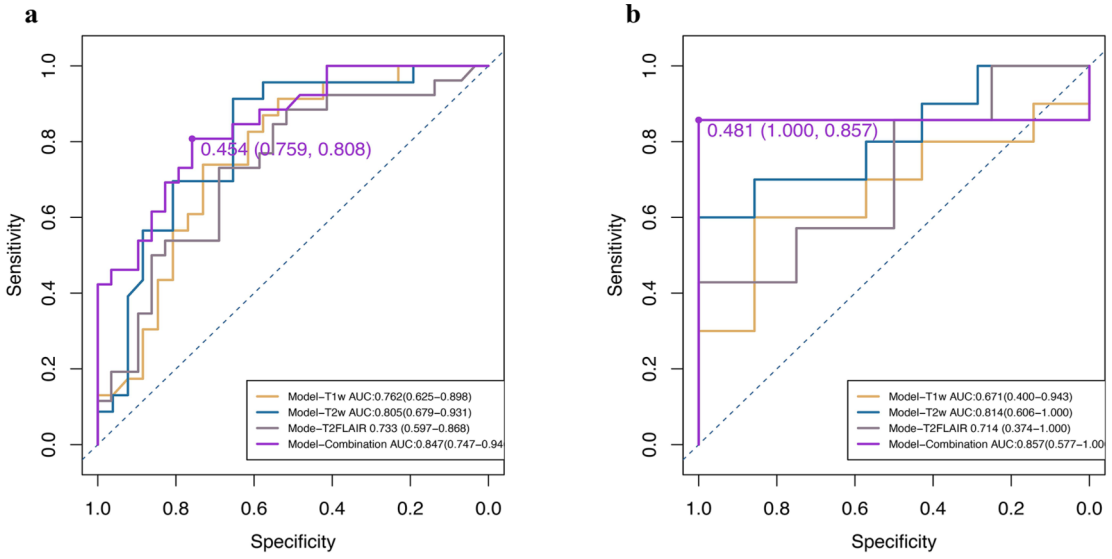

Fig. 4 ROC curves of the four diagnostic models in the training (**a**) and validation sets (**b**). The yellow curve represents Model-T1w, the blue curve represents Model-T2w, the gray curve represents Model-T2FLAIR, and the purple curve represents Model-Combination

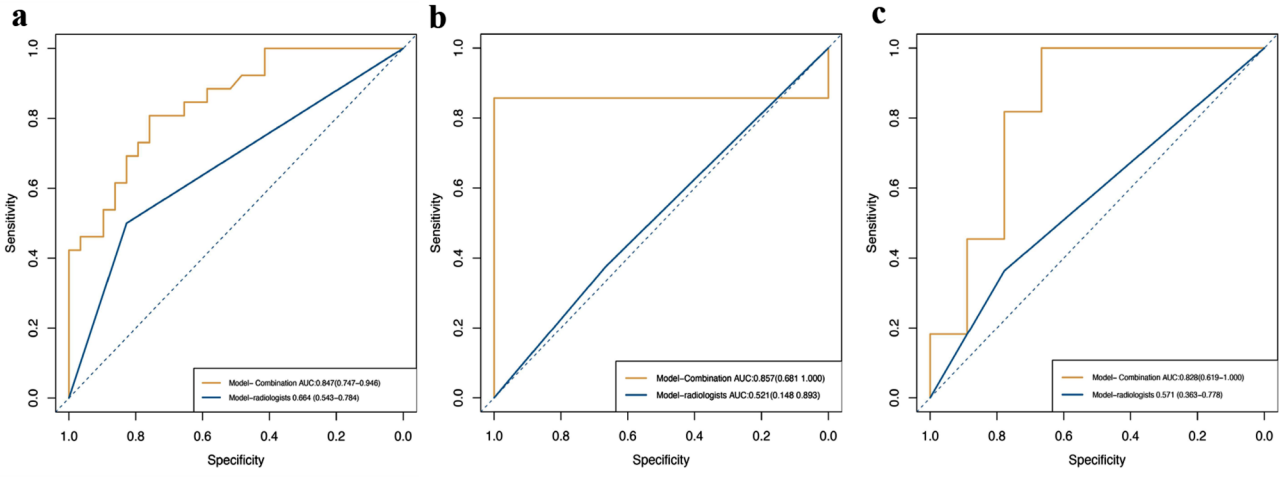

Fig. 5 ROC curves of Model-Combination and Model-radiologist in the training (**a**), validation (**b**), and hold-out sets (**c**). The yellow curve represents Model-Combination, and the blue curve represents the Model-radiologists

other models in the training and validation sets and outperformed diagnosis made by an inexperienced radiologist in the training (AUCs: 0.847 VS. 0.664, $p=0.008$) and validation (AUC: 0.618 VS. 0.521, $p=0.155$) sets. Notably, the combined model exhibited robust performance in diagnosing FCD and was further used to determine the laterality of the lesion in the hold-out set (AUC: 0.828 VS. 0.571, $p=0.080$). In addition, we explored the correlation between the selected significant features and the duration of FCD and observed that only the correlation of log-sigma-1-0-mm-3D_ngtdm_Contrast had statistical significance (r = -0.319, $p<0.05$), indicating that this feature could help identify FCD in MRI visual detection.

When comparing the performance of models based on the single sequence, we discovered that the model based on the T2w sequence performed best, which was consistent with Colombo and House's studies about the MR evaluation of FCD [36, 37]. T2w imaging was superior to T1w imaging in identifying lesions, with increased T2 relaxation times for almost any change in brain tissue composition, while extended T1 relaxation times occurred only in some visible lesions [38]. In terms of FCD, T2w imaging uses slices to acquire images that most clearly outline the morphology of the GM/WM junction, thus facilitating the evaluation of cortical thickness. Even if the MRI resolution is far too coarse to discern individual neuronal profiles, cellular densities are likely to change T2 and FLAIR signals on high-resolution MRI [39]. Therefore, the T2w demonstrates its extreme superiority in FCD detection. T2w imaging reveals

Table 5 Reclassification among model-combination and model-radiologist in training, validation and hold-out sets

	Model-Combination VS. Model-radiologists		
		95%CI	*p* value
Training set:			
NRI(Categorical)	0.402	[0.064–0.740]	0.020
NRI(Continuous)	0.679	[0.183–1.175]	0.007
IDI	0.158	[0.043–0.273]	0.007
Validation set:			
NRI(Categorical)	0.607	[-0.029–1.243]	0.061
NRI(Continuous)	1.143	[0.410–1.876]	0.002
IDI	0.264	[0.012–0.517]	0.040
Hold-out set:			
NRI(Categorical)	0.424	[-0.164–1.012]	0.157
NRI(Continuous)	1.192	[0.484–1.901]	< 0.000
IDI	0.264	[0.046–0.482]	0.018

blurred gray–white matter boundaries, which may be the result of neuronal dispersion into the U-fiber layer, localized thinning or thickening of the cortex, impaired myelination, the presence of bizarre glial cells, ectopic neurons, and reduced numbers of myelinated fibers in the white matter [40]. Furthermore, T2w is the most suitable sequence for this evaluation at any age, particularly for neonates and infants aged < 6 months, whose cortical dysplasia is manifested by a high density of unmyelinated WM fibers [36, 41]. In previous studies on the appearance of FCD on MRI, FLAIR was also shown to be more sensitive in detecting lesions, but the model based on the T2FLAIR sequence in our study performed poorly. We hypothesized that this is because, specifically in FCD type IIb but not in other types of FCD, high signals in the gray matter and subwhite matter extending into the lateral ventricles (transmantle sign) were the most sensitive appearance of FCD on FLAIR. However, only three patients with FCD type IIb were included in our study (7.0% of the overall cohort); therefore, the benefits of FLAIR were not obvious. According to earlier research, T2w and FLAIR images are more effective than T1w images in detecting abnormal signals in white matter [42]. However, T1w volumetric acquisitions with isotropic 1 mm^3 voxels are ideal for analyzing variations in cortical thickness because of their thinner slices [43]. Consequently, using multiple sequences for radiomics analysis may contribute to lesion detection.

We discovered that the model based on the combination had the highest performance of all models and showed better diagnostic performance than inexperienced radiologists. In Model-Combination, a total of six features were selected as the optimal features: two features based on T1w imaging, three features based on T2w imaging, and one feature based on T2FLAIR imaging. The T2 wavelet-HHL_GLCM_correlation feature, which is part of the GLCM in texture features, ranked first in terms of weight. Correlation is a measure of the similarity of the elements of the spatial grayscale co-occurrence matrix in the row or column direction, reflecting the local grayscale correlation of the texture, and is greater when the values of some elements of the matrix are uniformly equal [44]. This method provides a more objective assessment of changes in MR images with scalar values than the human assessment of whether abnormal signals are present on MR imaging. The feature with the second-highest weight is ngtdm (log-sigma-1-0-mm-3D_Contrast), which quantifies the sum of differences between the gray level of a pixel or voxel and the mean gray level of its neighboring pixels or voxels within a predefined distance and reflects the variation around local voxels on T2w imaging [45].

These six features in this study consist of both histogram features that reflect the voxel intensity distribution of the lesion and texture features that reflect the local relationship between pixels or voxels, but unlike earlier studies in the field of radiomics in oncology, no shape-based features were selected. We supposed that this may be due to the method of segmentation used in this study. Most FCD lesions are MRI-negative, and even when they are positive, they are typically not well separated from the surrounding cerebral tissue. To better segment the lesions, we identified them based on the surgical area, potentially weakening the influence of shape-based features.

In addition, of the six optimal features selected for this study, only ngtdm (log-sigma-1-0-mm-3D_Contrast) had a positive, significant correlation with the duration of FCD. This contrast reflects how local voxels vary from their surroundings and is dependent on both spatial disparity and the total gray dynamic range, with high contrast representing a large gray dynamic range and spatial disparity in the lesion [46]. The results of our study also demonstrated that the contrast of the lesions decreased as the duration of FCD increased. This is also consistent with previous studies indicating that blurring of the gray–white matter junction is the most sensitive marker of FCD and is found in proportion to the severity of histopathological changes [47]. Therefore, this feature should be given additional attention in clinical practice or at least in future studies.

Our study had several limitations. Although we report satisfactory FCD detection accuracy in our cohort, the present study only represents a reasonable but not large cohort of subjects. Further validation of the method should include a larger dataset. Due to the relatively small sample size in this study, to further demonstrate the classification value of the model, this study utilized NRI and IDI indices. However, it is important to note that large values for the NRI statistic may simply be due to the use of poorly fitting risk models. Although, based

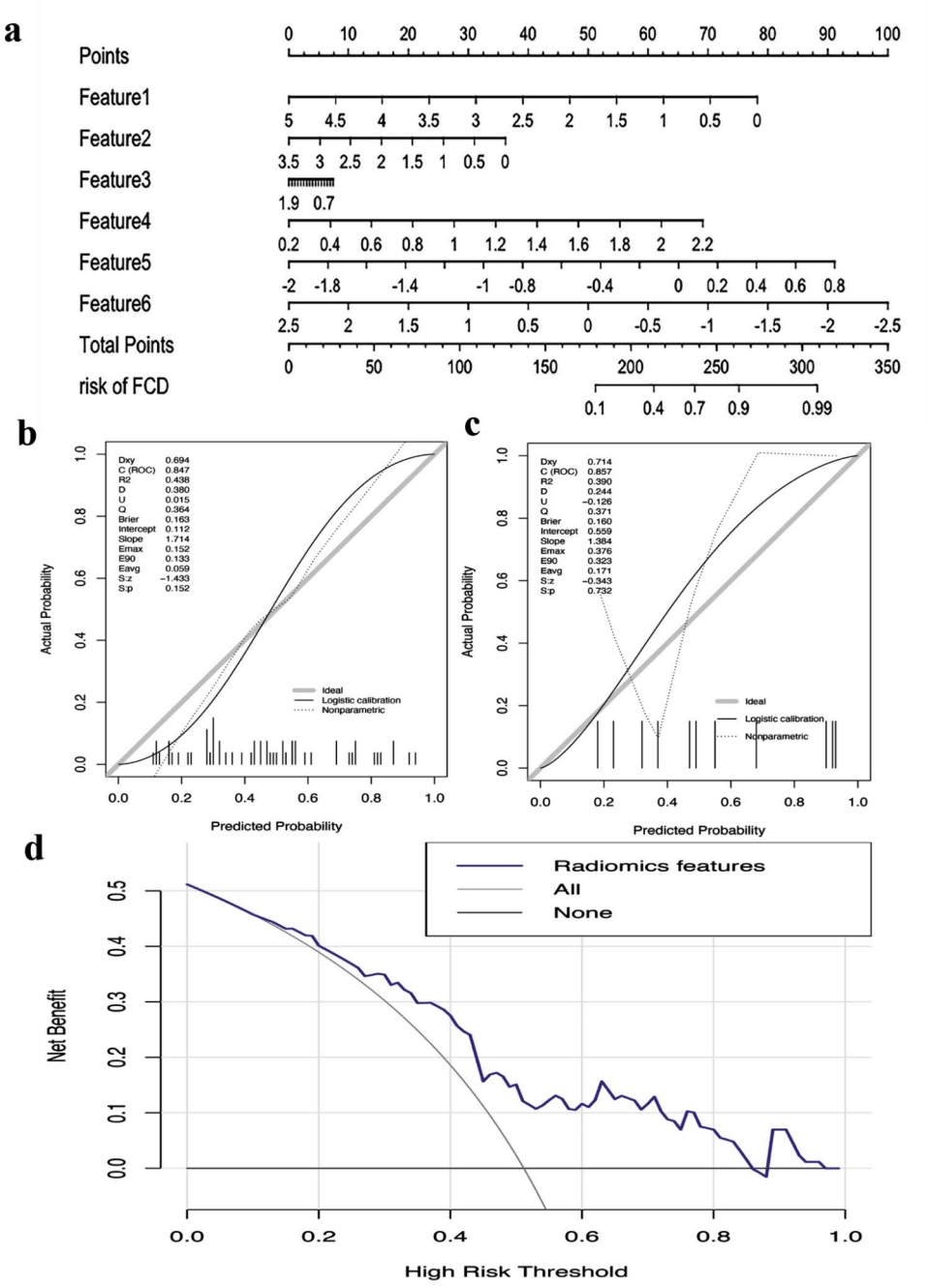

Fig. 6 The nomogram (**a**), calibration curves in the training (**b**) set, validation sets (**c**) and decision curve of the Model-Combination (**d**). **(a)** The Model-Combination radiomics nomogram integrated the six features extracted and selected from combined (T1w+T2w+FLAIR) images. Feature 1: T2_log-sigma-1-0-mm-3D_gldm_DependenceVariance; Feature 2: T1_wavelet-HLLgldm_LargeDependenceLowGrayLevelEmphasis; Feature 3: T2FLAIR_log-sigma-0-5-mm-3D_firstorder_Median; Feature 4: T1_wavelet-HLLglszm_ZoneVariance; Feature 5: T2_log-sigma-1-0-mm-3D_ngtdm_Contrast; Feature 6: T2_wavelet-HHL_glcm_Correlation. (**b**, **c**) Calibration curves of Model-Combination in the training set and validation set. The diagonal gray line represents a perfect diagnosis by an ideal model. The black solid line represents the diagnostic performance of the Model-Combination; the closer the black line is to the gray line, the better the diagnostic performance of the model. (**d**) Decision curve for the nomogram diagnosing FCD in the overall patients. The y-axis represents the net benefit. The purple line represents the diagnostic nomogram model. The gray line represents the assumption that all patients have FCD. The black line represents the assumption that no patients have FCD

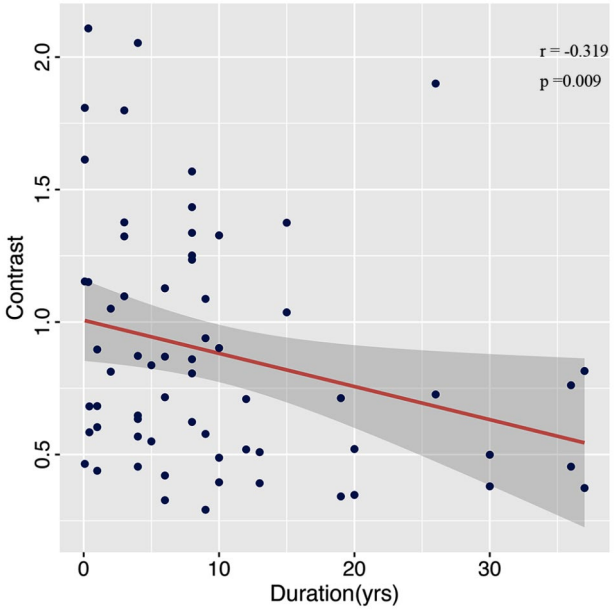

Fig. 7 Correlation analysis between the contrast (the radiomics feature belongs to texture features) and duration of FCD. The blue dots represent data, the red curve represents the fitted curve, and the gray areas represent the 95% confidence interval (CI)

on the MSE and R^2 values, the model's fitting ability is not very poor, there are still certain limitations to the NRI index. This also contributes to the statistical weaknesses of this study. Second, compared to conventional machine learning (ML), deep learning (DL) has advantages in computation, as a high-performance graphics processing unit (GPU) supports fast computing and less time spent on modeling. Similar to end-to-end learning, DL can automatically extract relevant functions from images, and tasks such as raw data processing and classification can be completed automatically [48, 49]. However, DL is complex and requires thousands of images at the start; the risk of overfitting is greater if the sample size is small. Therefore, classical ML methods meet our needs and fit the data. In future research, we will obtain a larger number of samples and adopt deep learning algorithms to build more accurate and robust models. Third, we only performed initial lateralization of FCD lesions but were not yet able to achieve localization, which is the direction and goal of our subsequent research.

In conclusion, the radiomics nomogram was generated by logistic regression model-based multiparametric MRI and facilitated the diagnosis of FCD. When surgical treatment was chosen, our model could be used to further determine the laterality of the lesion to aid in preoperative evaluation. Our study represents an important advance in the diagnosis and treatment of FCD.

Supplementary Information

The online version contains supplementary material available at https://doi.org/10.1186/s12880-024-01374-6.

Supplementary Material 1
Supplementary Material 2
Supplementary Material 3
Supplementary Material 4
Supplementary Material 5
Supplementary Material 6
Supplementary Material 7
Supplementary Material 8
Supplementary Material 9
Supplementary Material 10

Acknowledgements
Not applicable.

Author contributions
Shiqi Chen and Liang Wei contributed equally to this work. Conception and design of the research: SQ-C. Acquisition of data: LW, KH.Data curation, Investigation: YW-X, ZT-Z. Statistical analysis: TS, DW, YL, YF-G. Funding acquisition: XY-S. Critical revision of the manuscript for intellectual content: XL-X and JK-D. All authors read and approved the final manuscript.

Funding
Funding was provided by grants from the Youth Research Project of Jiangxi Science and Technology Department (20171BAB215049). Funding Acquisition: XY-S.

Data availability
The radiomics data are attached as Supplementary Materials 7, and the code is attached as Supplementary Materials 9. The raw MR images used and analyzed during the current study are available from the corresponding author upon reasonable request. The data are not publicly available due to information that could compromise the privacy of research participants.

Declarations

Ethics approval and consent to participate
The institutional review board of the Second Affiliated Hospital of Nanchang University approved this retrospective study. The need for informed consent was waived by the ethics committee Review Board of the Second Affiliated Hospital of Nanchang University because of the retrospective nature of the study. All methods were carried out in accordance with relevant guidelines and regulations or the Declaration of Helsinki.

Consent for publication
Not applicable.

Conflict of interest
No conflict of interest exists in the submission of this manuscript.

Author details
[1]Department of Radiology, The Second Affiliated Hospital of Nanchang University, Nanchang, Jiangxi Province, China
[2]Department of Pediatrics, The Affiliated Hospital of Jinggangshan University, Jinggangshan, Jiangxi Province, China
[3]GE Healthcare, MR Research China, Beijing, China

Received: 26 November 2022 / Accepted: 22 July 2024
Published online: 15 August 2024

References

1. De Vito A, Mankad K, Pujar S, Chari A, Ippolito D, D'Arco F. Narrative review of epilepsy: getting the most out of your neuroimaging. Transl Pediatr. 2021;10(4):1078–99.
2. Blumcke I, Thom M, Aronica E, Armstrong DD, Vinters HV, Palmini A, Jacques TS, Avanzini G, Barkovich AJ, Battaglia G, et al. The clinicopathologic spectrum of focal cortical dysplasias: a consensus classification proposed by an ad hoc Task Force of the ILAE Diagnostic Methods Commission. Epilepsia. 2011;52(1):158–74.
3. Taylor DC, Falconer MA, Bruton CJ, Corsellis JA. Focal dysplasia of the cerebral cortex in epilepsy. J Neurol Neurosurg Psychiatry. 1971;34(4):369–87.
4. Veersema TJ, Swampillai B, Ferrier CH, van Eijsden P, Gosselaar PH, van Rijen PC, Spliet WGM, Muhlebner A, Aronica E, Braun KPJ. Long-term seizure outcome after epilepsy surgery in patients with mild malformation of cortical development and focal cortical dysplasia. Epilepsia Open. 2019;4(1):170–5.
5. Fisher RS, Acevedo C, Arzimanoglou A, Bogacz A, Cross JH, Elger CE, Engel J Jr., Forsgren L, French JA, Glynn M, et al. ILAE official report: a practical clinical definition of epilepsy. Epilepsia. 2014;55(4):475–82.
6. Middlebrooks EH, Lin C, Westerhold E, Okromelidze L, Vibhute P, Grewal SS, Gupta V. Improved detection of focal cortical dysplasia using a novel 3D imaging sequence: edge-enhancing gradient Echo (3D-EDGE) MRI. Neuroimage Clin. 2020;28:102449.
7. Martin P, Bender B, Focke NK. Post-processing of structural MRI for individualized diagnostics. Quant Imaging Med Surg. 2015;5(2):188–203.
8. Kini LG, Gee JC, Litt B. Computational analysis in epilepsy neuroimaging: a survey of features and methods. Neuroimage Clin. 2016;11:515–29.
9. Bernasconi A, Antel SB, Collins DL, Bernasconi N, Olivier A, Dubeau F, Pike GB, Andermann F, Arnold DL. Texture analysis and morphological processing of magnetic resonance imaging assist detection of focal cortical dysplasia in extra-temporal partial epilepsy. Ann Neurol. 2001;49(6):770–5.
10. Colliot O, Bernasconi N, Khalili N, Antel SB, Naessens V, Bernasconi A. Individual voxel-based analysis of gray matter in focal cortical dysplasia. NeuroImage. 2006;29(1):162–71.
11. Pail M, Marecek R, Hermanova M, Slana B, Tyrlikova I, Kuba R, Brazdil M. The role of voxel-based morphometry in the detection of cortical dysplasia within the temporal Pole in patients with intractable mesial temporal lobe epilepsy. Epilepsia. 2012;53(6):1004–12.
12. Thesen T, Quinn BT, Carlson C, Devinsky O, DuBois J, McDonald CR, French J, Leventer R, Felsovalyi O, Wang X, et al. Detection of epileptogenic cortical malformations with surface-based MRI morphometry. PLoS ONE. 2011;6(2):e16430.
13. Huppertz HJ, Wellmer J, Staack AM, Altenmuller DM, Urbach H, Kroll J. Voxel-based 3D MRI analysis helps to detect subtle forms of subcortical band heterotopia. Epilepsia. 2008;49(5):772–85.
14. Fischl B, Sereno MI, Dale AM. Cortical surface-based analysis. II: inflation, flattening, and a surface-based coordinate system. NeuroImage. 1999;9(2):195–207.
15. Dale AM, Fischl B, Sereno MI. Cortical surface-based analysis. I. Segmentation and surface reconstruction. NeuroImage. 1999;9(2):179–94.
16. Besson P, Bernasconi N, Colliot O, Evans A, Bernasconi A. Surface-based texture and morphological analysis detects subtle cortical dysplasia. Med Image Comput Comput Assist Interv. 2008;11(Pt 1):645–52.
17. Giuliani NR, Calhoun VD, Pearlson GD, Francis A, Buchanan RW. Voxel-based morphometry versus region of interest: a comparison of two methods for analyzing gray matter differences in schizophrenia. Schizophr Res. 2005;74(2–3):135–47.
18. Lambin P, Rios-Velazquez E, Leijenaar R, Carvalho S, van Stiphout RG, Granton P, Zegers CM, Gillies R, Boellard R, Dekker A, et al. Radiomics: extracting more information from medical images using advanced feature analysis. Eur J Cancer. 2012;48(4):441–6.
19. Yin F, Yan X, Gao R, Ren Z, Yu T, Zhao Z, Zhang G. Radiomics features from 3D-MPRAGE imaging can differentiate temporal-plus epilepsy from temporal lobe epilepsy. Epileptic Disord 2023.
20. Park YW, Choi YS, Kim SE, Choi D, Han K, Kim H, Ahn SS, Kim SA, Kim HJ, Lee SK, et al. Radiomics features of hippocampal regions in magnetic resonance imaging can differentiate medial temporal lobe epilepsy patients from healthy controls. Sci Rep. 2020;10(1):19567.
21. Cheong EN, Park JE, Jung DE, Shim WH. Extrahippocampal Radiomics Analysis can potentially identify laterality in patients with MRI-Negative temporal lobe Epilepsy. Front Neurol. 2021;12:706576.
22. Hu Z, Jiang D, Zhao X, Yang J, Liang D, Wang H, Zhao C, Liao J. Predicting Drug Treatment outcomes in Childrens with Tuberous Sclerosis Complex-Related Epilepsy: a clinical Radiomics Study. AJNR Am J Neuroradiol. 2023;44(7):853–60.
23. Owen TW, de Tisi J, Vos SB, Winston GP, Duncan JS, Wang Y, Taylor PN. Multivariate white matter alterations are associated with epilepsy duration. Eur J Neurosci. 2021;53(8):2788–803.
24. Banks J. Nomograms. Encylopedia of Statistical Sciences, vol. 6. *New York, NY: Wiley* 1985.
25. Fauser S, Essang C, Altenmuller DM, Staack AM, Steinhoff BJ, Strobl K, Bast T, Schubert-Bast S, Stephani U, Wiegand G, et al. Long-term seizure outcome in 211 patients with focal cortical dysplasia. Epilepsia. 2015;56(1):66–76.
26. Wieser HG, Blume WT, Fish D, Goldensohn E, Hufnagel A, King D, Sperling MR, Luders H, Pedley TA, Commission on Neurosurgery of the International League Against E. ILAE Commission Report. Proposal for a new classification of outcome with respect to epileptic seizures following epilepsy surgery. Epilepsia. 2001;42(2):282–6.
27. Durnford AJ, Rodgers W, Kirkham FJ, Mullee MA, Whitney A, Prevett M, Kinton L, Harris M, Gray WP. Very good inter-rater reliability of Engel and ILAE Epilepsy surgery outcome classifications in a series of 76 patients. Seizure. 2011;20(10):809–12.
28. Kocak B, Baessler B, Bakas S, Cuocolo R, Fedorov A, Maier-Hein L, Mercaldo N, Muller H, Orlhac F, Pinto Dos Santos D, et al. CheckList for EvaluAtion of Radiomics research (CLEAR): a step-by-step reporting guideline for authors and reviewers endorsed by ESR and EuSoMII. Insights Imaging. 2023;14(1):75.
29. Smith SM. Fast robust automated brain extraction. Hum Brain Mapp. 2002;17(3):143–55.
30. Zwanenburg A, Vallieres M, Abdalah MA, Aerts H, Andrearczyk V, Apte A, Ashrafinia S, Bakas S, Beukinga RJ, Boellaard R, et al. The image Biomarker Standardization Initiative: standardized quantitative Radiomics for High-Throughput Image-based phenotyping. Radiology. 2020;295(2):328–38.
31. Tibshirani R. The lasso method for variable selection in the Cox model. Stat Med. 1997;16(4):385–95.
32. Iasonos A, Schrag D, Raj GV, Panageas KS. How to build and interpret a nomogram for cancer prognosis. J Clin Oncol. 2008;26(8):1364–70.
33. Vickers AJ, Elkin EB. Decision curve analysis: a novel method for evaluating prediction models. Med Decis Mak. 2006;26(6):565–74.
34. Pencina MJ, D'Agostino RB, Sr., D'Agostino RB Jr., Vasan RS. Evaluating the added predictive ability of a new marker: from area under the ROC curve to reclassification and beyond. Stat Med. 2008;27(2):157–72. discussion 207 – 112.
35. Lambin P, Leijenaar RTH, Deist TM, Peerlings J, de Jong EEC, van Timmeren J, Sanduleanu S, Larue R, Even AJG, Jochems A, et al. Radiomics: the bridge between medical imaging and personalized medicine. Nat Rev Clin Oncol. 2017;14(12):749–62.
36. Colombo N, Tassi L, Deleo F, Citterio A, Bramerio M, Mai R, Sartori I, Cardinale F, Lo Russo G, Spreafico R. Focal cortical dysplasia type IIa and IIb: MRI aspects in 118 cases proven by histopathology. Neuroradiology. 2012;54(10):1065–77.
37. House PM, Lanz M, Holst B, Martens T, Stodieck S, Huppertz HJ. Comparison of morphometric analysis based on T1- and T2-weighted MRI data for visualization of focal cortical dysplasia. Epilepsy Res. 2013;106(3):403–9.
38. Barkhof F, van Walderveen M. Characterization of tissue damage in multiple sclerosis by nuclear magnetic resonance. Philos Trans R Soc Lond B Biol Sci. 1999;354(1390):1675–86.
39. Muhlebner A, Coras R, Kobow K, Feucht M, Czech T, Stefan H, Weigel D, Buchfelder M, Holthausen H, Pieper T, et al. Neuropathologic measurements in focal cortical dysplasias: validation of the ILAE 2011 classification system and diagnostic implications for MRI. Acta Neuropathol. 2012;123(2):259–72.
40. Yagishita A, Arai N, Maehara T, Shimizu H, Tokumaru AM, Oda M. Focal cortical dysplasia: appearance on MR images. Radiology. 1997;203(2):553–9.
41. Deblaere K, Achten E. Structural magnetic resonance imaging in epilepsy. Eur Radiol. 2008;18(1):119–29.
42. Focke NK, Symms MR, Burdett JL, Duncan JS. Voxel-based analysis of whole brain FLAIR at 3T detects focal cortical dysplasia. Epilepsia. 2008;49(5):786–93.
43. Kulaseharan S, Aminpour A, Ebrahimi M, Widjaja E. Identifying lesions in paediatric epilepsy using morphometric and textural analysis of magnetic resonance images. Neuroimage Clin. 2019;21:101663.
44. Shafiq-Ul-Hassan M, Zhang GG, Latifi K, Ullah G, Hunt DC, Balagurunathan Y, Abdalah MA, Schabath MB, Goldgof DG, Mackin D, et al. Intrinsic dependencies of CT radiomic features on voxel size and number of gray levels. Med Phys. 2017;44(3):1050–62.
45. Amadasun M, King R. Textural features corresponding to textural properties. IEEE Trans Syst Man Cybernetics. 1989;19(5):1264–74.

46. Mayerhoefer ME, Materka A, Langs G, Haggstrom I, Szczypinski P, Gibbs P, Cook G. Introduction to Radiomics. J Nucl Med. 2020;61(4):488–95.
47. Krsek P, Maton B, Korman B, Pacheco-Jacome E, Jayakar P, Dunoyer C, Rey G, Morrison G, Ragheb J, Vinters HV, et al. Different features of histopathological subtypes of pediatric focal cortical dysplasia. Ann Neurol. 2008;63(6):758–69.
48. McBee MP, Awan OA, Colucci AT, Ghobadi CW, Kadom N, Kansagra AP, Tridandapani S, Auffermann WF. Deep learning in Radiology. Acad Radiol. 2018;25(11):1472–80.
49. Zhao X, Zhao XM. Deep learning of brain magnetic resonance images: a brief review. Methods. 2021;192:131–40.

Publisher's Note